

See discussions, stats, and author profiles for this publication at: <https://www.researchgate.net/publication/256200192>

# Au-Cu<sub>2-x</sub>Se Heterodimer Nanoparticles with Broad Localized Surface Plasmon Resonance as Contrast Agents for Deep Tissue Imaging (Vol 13, Pg 4333, 2013)

ARTICLE *in* NANO LETTERS · AUGUST 2013

Impact Factor: 13.59 · DOI: 10.1021/nl402124h · Source: PubMed

CITATIONS

42

READS

83

10 AUTHORS, INCLUDING:



**Changho Lee**

Pohang University of Science and Technology

36 PUBLICATIONS 160 CITATIONS

SEE PROFILE



**Wing-Cheung Law**

University at Buffalo, The State University of N...

79 PUBLICATIONS 2,470 CITATIONS

SEE PROFILE



**Chulhong Kim**

University at Buffalo, The State University of N...

96 PUBLICATIONS 2,876 CITATIONS

SEE PROFILE



**Mark Swihart**

University at Buffalo, The State University of N...

213 PUBLICATIONS 6,131 CITATIONS

SEE PROFILE

# Au–Cu<sub>2–x</sub>Se Heterodimer Nanoparticles with Broad Localized Surface Plasmon Resonance as Contrast Agents for Deep Tissue Imaging

Xin Liu,<sup>†</sup> Changho Lee,<sup>‡,§,¶</sup> Wing-Cheung Law,<sup>||,⊥</sup> Dewei Zhu,<sup>†,||</sup> Maixian Liu,<sup>||,#</sup> Mansik Jeon,<sup>‡</sup> Jeehyun Kim,<sup>§</sup> Paras N. Prasad,<sup>\*,||,#,∇</sup> Chulhong Kim,<sup>\*,‡,¶</sup> and Mark T. Swihart<sup>\*,†,||</sup>

<sup>†</sup>Department of Chemical and Biological Engineering, University at Buffalo (SUNY), Buffalo, New York 14260, United States

<sup>‡</sup>Department of Biomedical Engineering, University at Buffalo (SUNY), Buffalo, New York 14260, United States

<sup>§</sup>Department of Electrical and Computer Engineering, Kyungpook National University, Daegu, Republic of Korea 702-701

<sup>||</sup>Institute for Lasers, Photonics, and Biophotonics, University at Buffalo (SUNY), Buffalo, New York 14260, United States

<sup>⊥</sup>Department of Industrial and Systems Engineering, The Hong Kong Polytechnic University, Hung Hom, Kowloon, Hong Kong, P. R. China

<sup>#</sup>Department of Chemistry, University at Buffalo (SUNY), Buffalo, New York 14260, United States

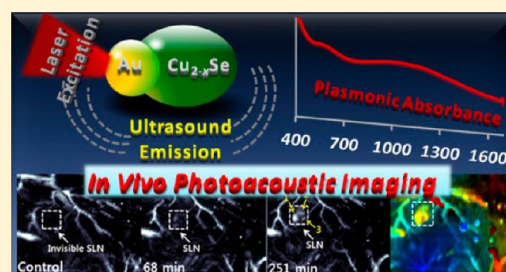
<sup>∇</sup>Department of Chemistry, Korea University, Seoul 136-701, Korea

<sup>¶</sup>Department of Creative IT Engineering, Pohang University of Science and Technology (POSTECH), Pohang, Gyeongbuk, Republic of Korea 790-784

## S Supporting Information

**ABSTRACT:** We report a new type of heterogeneous nanoparticles (NPs) composed of a heavily doped semiconductor domain (Cu<sub>2–x</sub>Se) and a metal domain (Au), which exhibit a broad localized surface plasmon resonance (LSPR) across visible and near-infrared (NIR) wavelengths, arising from interactions between the two nanocrystal domains. We demonstrate both in vivo photoacoustic imaging and in vitro dark field imaging, using the broad LSPR in Cu<sub>2–x</sub>Se–Au hybrid NPs to achieve contrast at different wavelengths. The high photoacoustic imaging depth achieved, up to 17 mm, shows that these novel contrast agents could be clinically relevant. More broadly, this work demonstrates a new strategy for tuning LSPR absorbance by engineering the density of free charge carriers in two interacting domains.

**KEYWORDS:** Localized surface plasmon resonance, heavily doped semiconductor, photoacoustic imaging, metal nanoparticles, contrast agent



Over the past decade, nanoparticle (NP)-based bioimaging techniques have undergone remarkable development,<sup>1–5</sup> harnessing the unique advantages of nanoparticles over conventional molecular contrast agents in specific applications. Metallic nanostructures,<sup>3,6,7</sup> semiconductor nanocrystals,<sup>1,2,8–10</sup> and magnetic nanoparticles<sup>11–13</sup> have each been developed as robust and effective contrast agents and probes for different imaging modalities. Size,<sup>14,15</sup> shape,<sup>16–18</sup> and composition<sup>19,20</sup> of such nanomaterials can be tuned to achieve enhanced imaging contrast as well as targeted delivery and therapy.<sup>18,21–23</sup> Recently, contrast agents for multimodal imaging have been developed by integrating NPs that provide image contrast based on different properties, including optical, electronic, and magnetic properties. These general methodologies for coupling materials with different functionalities can involve coencapsulation,<sup>24–26</sup> conjugation of separate NPs using linker molecules, or direct growth of one type of NP on the other in a core–shell or dumbbell geometry.<sup>27,28</sup> The

heterogeneous NPs synthesized by the latter protocol are smaller in size, which can promote cell internalization, diffusion and circulation in vivo. However, in this direct growth approach, the original properties of each component are usually impaired or even sacrificed.<sup>29,30</sup>

Representative inorganic heterogeneous NPs include metal–magnetic and metal–semiconductor combinations. For example, Fe<sub>3</sub>O<sub>4</sub>–Au hybrid NPs<sup>30</sup> combine magnetic and plasmonic properties that potentially allow their simultaneous use as contrast agents for magnetic resonance imaging (MRI) and optical imaging. However, in many semiconductor–metal nanodimer structures, the essential optical property of the semiconductor domain, usually photoluminescence, is compromised by the presence of the metal domain. This can be

**Received:** June 11, 2013

**Revised:** August 16, 2013

**Published:** August 28, 2013

attributed to nonradiative recombination via interface states or to exciton or charge transfer from the semiconductor domain to the metallic domain. For example, in Au–CdSe,<sup>29</sup> Au–CdS,<sup>31,32</sup> and Au–PbS<sup>30</sup> heterodimers, the PL emission from the semiconductor domain was quenched by the Au nanocrystal domain. The accompanying observation of a shift of LSPR wavelength of the metal domain may result from formation of interfacial electronic states, the high refractive index of the semiconductor domain, and/or delocalization of plasmons. These semiconductor–metal hybrid nanoparticles are prototypes used in fundamental studies of physical processes including charge transfer at semiconductor–metal quantum junctions and the interactions between excitons and plasmons.

Recently, LSPR was observed in heavily doped semiconductors. The prototypical examples of this are self-doped copper chalcogenide ( $\text{Cu}_{2-x}\text{Se}$  and  $\text{Cu}_{2-x}\text{S}$ ) NPs.<sup>33–36</sup> In contrast to LSPR in metals, which is attributed to oscillation of free electrons, the LSPR in these heavily doped copper chalcogenide NPs arises from free holes. Cation vacancies in these copper-deficient Cu(I) chalcogenides are the source of these free holes. The strong near-infrared (NIR) LSPR absorbance of these self-doped semiconductor NPs has recently been shown to provide deep tissue contrast enhancement for photoacoustic (PA) imaging. A robust PA signal from a sentinel lymph node of a rat was detected at a depth of about 3.5 mm using phospholipid–poly(ethylene glycol) encapsulated  $\text{Cu}_{2-x}\text{Se}$  NPs as a contrast agent.<sup>37</sup>

In the work reported here, we present a novel method for coupling heavily doped p-type copper selenide ( $\text{Cu}_{2-x}\text{Se}$ ) NPs with Au NPs by seeded nanocrystal growth to form a new type of semiconductor–metal heterogeneous NP. The main feature of this heterodimer nanostructure is that it simultaneously shows two types of LSPR in a single system. The Au– $\text{Cu}_{2-x}\text{Se}$  NPs exhibit a broad optical absorption that is nearly flat across the near-infrared (NIR) spectral region (750–1150 nm), along with a small shoulder at 566 nm that originates from the Au NP. This spectrum is significantly different from that of the Au NPs and from that of our previously reported  $\text{Cu}_{2-x}\text{Se}$  NPs. Moreover, we show the potential of utilizing the LSPR in Au– $\text{Cu}_{2-x}\text{Se}$  NPs for multimodal imaging, including deep tissue photoacoustic imaging in vivo and dark field optical imaging in vitro. This development opens a pathway to the rational engineering of the LSPR absorbance spectrum by judicious combination of plasmonic metal nanoparticles with heavily doped semiconductor NPs. This approach is substantially different from the methods generally used for tailoring LSPR by controlling the size and the shape of metal nanostructures or by using a core–shell geometry and allows one to achieve uniform absorbance across a broad spectrum using nanostructures that are much smaller than the gold nanorods, nanoshells, and nanocages that have often been used to create strong near-IR absorbers.

To synthesize Au– $\text{Cu}_{2-x}\text{Se}$  heterogeneous NPs, we used Au NPs of two representative sizes, 2.6 and 4.6 nm in diameter, as seeds for growth of  $\text{Cu}_{2-x}\text{Se}$  nanocrystal (NC) domains, producing heterodimer nanoparticles. A selenium precursor was prepared by dissolving selenium (Se) powder in oleic acid (OA) as described previously.<sup>35</sup> Use of OA–Se rather than alkylphosphine–Se as the precursor increases the concentration of cation vacancies (i.e., increases the value of  $x$ ) in  $\text{Cu}_{2-x}\text{Se}$  NC. Moreover, we observed that the OA–Se precursor facilitates controlled growth of the  $\text{Cu}_{2-x}\text{Se}$  crystal domain on

the Au NPs. The copper precursor was prepared by dissolving copper(I) chloride (CuCl) in oleylamine (OAm), then mixing it with the Au NP dispersion. The solution became black immediately after injecting OA–Se precursor into the mixture of copper precursor and Au NPs at 120 °C. The reaction temperature was gradually increased to 168 °C at a rate of 6–8 °C min<sup>−1</sup>. This led to nucleation and growth of a  $\text{Cu}_{2-x}\text{Se}$  nanocrystal domain on each Au seed, to produce a population of nearly identical Au– $\text{Cu}_{2-x}\text{Se}$  heterodimer NCs.

Transmission electron microscopy (TEM, Figure 1) revealed a dimer-like morphology of Au– $\text{Cu}_{2-x}\text{Se}$  heterogeneous NPs.

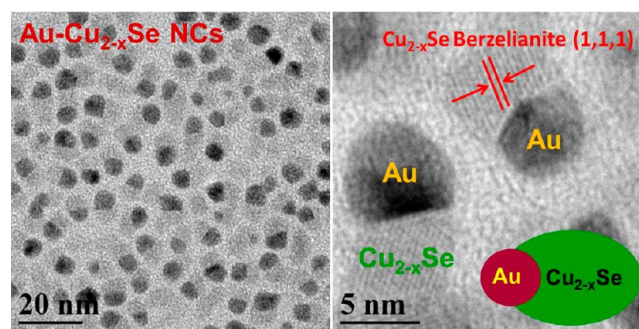


**Figure 1.** TEM and HRTEM images of Au– $\text{Cu}_{2-x}\text{Se}$  heterogeneous NPs.

The NPs prepared using ~4.6 nm Au seeds consisted of Au domains of 4.6–5 nm diameter and  $\text{Cu}_{2-x}\text{Se}$  domains of 6–7 nm diameter. High-resolution TEM (HRTEM) imaging of lattice planes in the  $\text{Cu}_{2-x}\text{Se}$  domain gave a lattice spacing of 0.33 nm, corresponding to {111} crystal planes of the berzelianite crystal phase. Powder X-ray diffraction (XRD, Figure 2) revealed the existence of face-centered cubic gold and berzelianite  $\text{Cu}_{2-x}\text{Se}$  crystal phases. The elemental composition of  $\text{Cu}_{2-x}\text{Se}$  was determined using energy-dispersive X-ray spectroscopy (EDS). The result showed that the atomic ratio of copper to selenium was 1.87 ( $x \approx 0.13$ ) demonstrating the high copper deficiency in the  $\text{Cu}_{2-x}\text{Se}$  nanocrystal domains. We analyzed the change of optical absorbance by comparing optical absorbance of Au– $\text{Cu}_{2-x}\text{Se}$  heterogeneous NPs with the original Au NPs. Initially, no distinct peak was observed for 2.6 nm Au NPs and a LSPR peak centered at 527 nm was detected for 4.6 nm NPs. The LSPR absorbance in Au– $\text{Cu}_{2-x}\text{Se}$  heterogeneous NPs exhibited broader and flatter peaks compared to pure Au NPs (Figure 3A). The Au– $\text{Cu}_{2-x}\text{Se}$  heterogeneous NCs synthesized using 4.6 nm Au had a LSPR peak that was red-shifted by 39 nm relative to the pure 4.6 nm Au NPs, to 566 nm (Figure 3A). A new plasmonic peak appeared at 558 nm (Figure S3) in the Au– $\text{Cu}_{2-x}\text{Se}$  heterogeneous NCs synthesized using 2.6 nm Au, although no distinct LSPR peak was present in the spectrum of the 2.6 nm Au NPs alone. In addition, we compared the absorbance of Au– $\text{Cu}_{2-x}\text{Se}$  heterogeneous NCs with pure  $\text{Cu}_{2-x}\text{Se}$  NCs (SI, Figure S4). The spectra were normalized to their values at the NIR absorbance peak centered at 1120 nm in pure  $\text{Cu}_{2-x}\text{Se}$  NCs. The Au– $\text{Cu}_{2-x}\text{Se}$  heterogeneous NCs show strong visible absorbance that is absent for the  $\text{Cu}_{2-x}\text{Se}$  NCs. This further illustrates that the absorbance spectrum of the Au– $\text{Cu}_{2-x}\text{Se}$  heterogeneous NC is not simply the sum of the absorbance spectra of the component homogeneous nanoparticles.

Moreover, the absorbance spectrum was extraordinarily flat across the NIR region ranging from 750 to 1150 nm, then



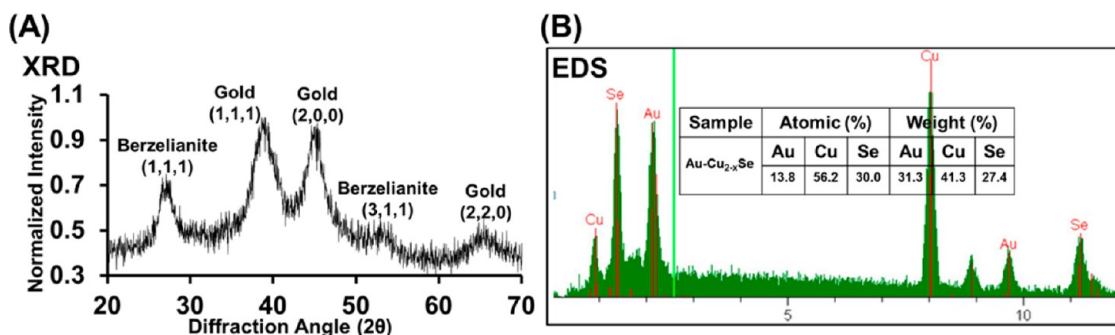


**Figure 2.** (A) XRD pattern showed the simultaneous existence of gold and copper selenide (berzelianite) crystal phases. (B) EDS analysis provides the relative amounts of Au, Cu, and Se in the heterogeneous nanoparticles.

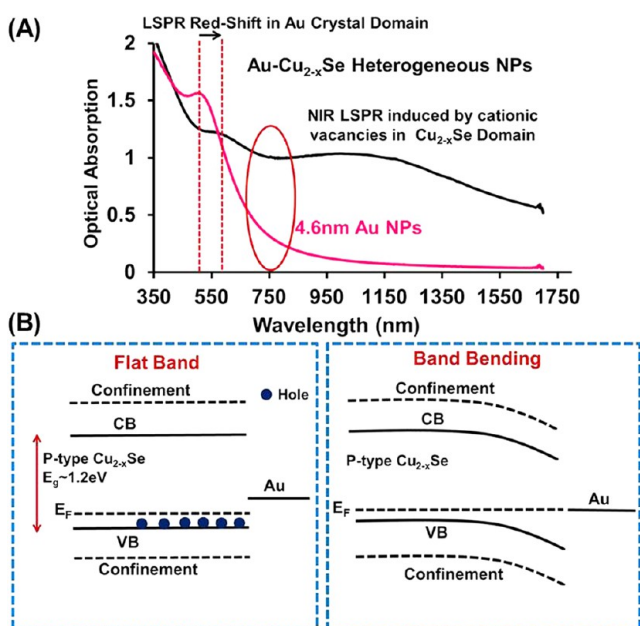


**Figure 3.** (A) Optical absorbance of 4.6 nm Au NPs and Au-Cu<sub>2-x</sub>Se heterogeneous NPs and (B) a schematic of the flat band alignment and band bending at the interface between Cu<sub>2-x</sub>Se and Au NC domains.

gradually decayed at longer wavelengths. This behavior is different from that of small Au NPs, which exhibit negligible absorption in the NIR spectral region. This longer wavelength optical absorption cannot be interpreted using theories usually applied to semiconductor-metal NPs. Instead, this NIR absorbance is attributed to the Cu<sub>2-x</sub>Se NC domains. The Cu<sub>2-x</sub>Se NCs prepared in this study have a high concentration of cation vacancies and therefore behave as a heavily doped p-type semiconductor. Such heavily doped Cu<sub>2-x</sub>Se NCs, in contrast to intrinsic or lightly doped semiconductor NCs, do not exhibit photoluminescence. However, the presence of a high concentration of free holes produces a LSPR absorbance in the Cu<sub>2-x</sub>Se NCs.

One can qualitatively analyze the interplay between the free electron-based LSPR in the Au domain and the free hole-based LSPR in the Cu<sub>2-x</sub>Se domain of the heterogeneous nanoparticles using a quantum junction model. The flat band diagram for this junction (Figure 3B) shows the Fermi level in the semiconductor domain close to the valence band maximum, due to the heavy p-type doping (cation vacancies). To achieve thermal equilibrium at the semiconductor-metal interface, diffusion of holes from the p-type semiconductor must occur,

to reach Fermi level alignment (Figure 3B). Due to the quantum size of the Au-Cu<sub>2-x</sub>Se NC, one can reasonably expect that holes could diffuse into the entire Au domain from the Cu<sub>2-x</sub>Se side. This decreases the electron density in the Au nanocrystal domain leading to a decreased absorbance cross-section and a red-shift of the LSPR wavelength. On the other hand, the NIR LSPR contributed by the Cu<sub>2-x</sub>Se nanocrystal domain was simultaneously depressed and broadened. This effect should be mainly attributed to the reduced hole concentration in the Cu<sub>2-x</sub>Se domain. For both materials, the LSPR wavelength depends upon the refractive index of the surrounding medium. The relatively high refractive index of Cu<sub>2-x</sub>Se will serve to red-shift the LSPR of the Au domain, while the low (real) refractive index of the gold, which is strongly wavelength-dependent but less than one throughout the NIR, will produce a blue-shift of the LSPR of the Cu<sub>2-x</sub>Se domain. The charge redistribution and interplay of refractive indices in Au-Cu<sub>2-x</sub>Se heterogeneous NCs provide a fundamentally new means of engineering the optical absorption spectrum of these materials through tailoring charge density in the NP domains.

Recently, LSPR in NPs has been utilized for photoacoustic tomography (PAT), an emerging noninvasive and nonionizing imaging method that is of great current interest.<sup>38–45</sup> To carry out imaging in the NIR window in which tissues are relatively transparent, metal NPs were synthesized with anisotropic shapes<sup>6,16,46</sup> and/or large sizes<sup>47</sup> that result in shifting their LSPR to the NIR region. Here, we demonstrate that these heterogeneous Au-Cu<sub>2-x</sub>Se nanoparticles can serve as contrast agents for PAT with exceptionally broad spectral response. Moreover, the broad absorption in Au-Cu<sub>2-x</sub>Se NPs allows the use of cost-effective laser sources (e.g., Nd:YAG laser at 1064 nm or various NIR diode lasers) for PAT.

The Cu<sub>2-x</sub>Se-Au NPs were made water-dispersible, for use in bioimaging, through ligand exchange using thiol-PEG. As compared with phospholipid-PEG encapsulated NPs, which would have larger hydrodynamic diameter, these PEGylated NPs disperse well in water while maintaining their small size, as demonstrated by TEM (Figure S5). A cytotoxicity study was executed using the MTS assay with macrophage cells. No toxicity was observed for the PEGylated NPs even for concentrations as high as 250  $\mu\text{g/mL}$  (Figure S6), demonstrating the high biocompatibility of these nanoparticles. The PEGylated NPs were then used for in vitro imaging using dark-field microscopy. Robust cellular uptake was observed. As shown in Figure S7, the PEGylated Cu<sub>2-x</sub>Se-Au NPs appear to accumulate in vesicles within the cells, suggesting an endocytotic uptake pathway.

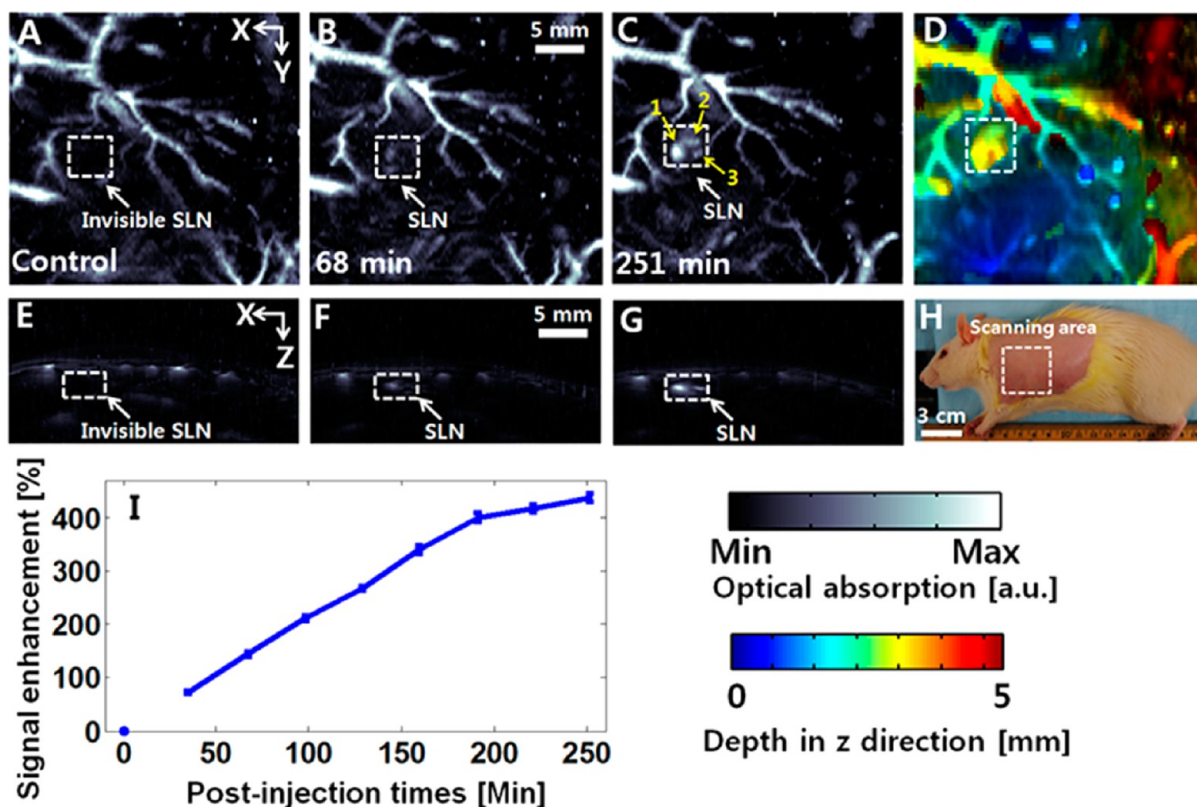


**Figure 4.** In vivo noninvasive photoacoustic (PA) time-course coronal MAP images. PA images were acquired before (A) and after (B–C) the Au–Cu<sub>2–x</sub>Se injection: (B) 68 min (SLN started to appear) and (C) 251 min after injection. Three lymph nodes indicated with 1–3 are visible in the axillary region. (D) Depth-encoded PA coronal MAP image of (C). (E–G) Depth-resolved cross-sectional PA B-scan images of A–C, respectively. (H) Photograph of an animal with hair removed before PA imaging. (I) Accumulations of Au–Cu<sub>2–x</sub>Se material in a SLN over time, in terms of the amplitude changes of PA signals. PA, photoacoustic and SLN, sentinel lymph node.

The photoacoustic sensitivity at 1064 nm was tested by measuring the photoacoustic signal amplitude of PEGylated Au–Cu<sub>2–x</sub>Se NPs in water at different concentrations. Measurements of the concentration-dependent photoacoustic signal (Figure S8) showed that the detection limit of the NPs was 100  $\mu\text{g/mL}$ , which is significantly below the maximum concentration at which biocompatibility was demonstrated in cytotoxicity assays.

The Au–Cu<sub>2–x</sub>Se nanoparticles were then used for sentinel lymph node (SLN) mapping in a rat using a reflection-mode photoacoustic imaging system with a wavelength of 1064 nm. Figure 4H shows a photograph of the rat before PA imaging. The white square marks the scanning area (30 mm  $\times$  30 mm). A control PA image (Figure 4A) was acquired before the injection of Au–Cu<sub>2–x</sub>Se in the forepaw pad. The vasculature under the skin surface was shown by a maximum amplitude projection (MAP). The sentinel node was not visible in the control PA image. After injecting Au–Cu<sub>2–x</sub>Se materials (4 mg/mL, 0.1 mL), the raster scanning began immediately, to capture the movement and accumulation of the Au–Cu<sub>2–x</sub>Se materials. The estimated blood volume in adult animals is 55–70 mL/kg body weight.<sup>48</sup> Thus, for a 250 g rat, the volume of blood is  $\sim$ 16 mL. Thus, at full dilution in the bloodstream, the in vivo concentration of NP was  $\sim$ 25  $\mu\text{g/mL}$ . In terms of the number of particles, the in vivo dose was estimated to  $2.6 \times 10^{11}$  particles/g body mass (SI). On the time scale of the in vitro cytotoxicity assays (48 to 72 h), the in vivo concentration at any particular location should drop well below the maximum concentration used in the in vitro assays. The PA signal from

the SLN appeared approximately 69 min after injection (Figure 4B). Relatively low contrast SLN images were acquired at that time point, reflecting low accumulation of Au–Cu<sub>2–x</sub>Se in the SLN. Figure 4C shows PA coronal MAP images acquired at 251 min after the injection. Interestingly, not only the sentinel node indicated with “1” but also other draining nodes indicated with “2” and “3” are delineated as shown in Figure 4C. This implies that the Au–Cu<sub>2–x</sub>Se NCs traveled through the lymphatic system and the axillary lymph node chain was photoacoustically detected in vivo. Figure 4E–G shows the depth-sensitive cross-sectional PA B-scan images of Figure 4A–C, respectively. Further, the depth information of the 251-min-postinjection PA MAP image (Figure 4C) was encoded using a pseudo color scheme as shown in Figure 4D. The location of the SLN ( $\sim$ 2 mm deep) accumulated with Au–Cu<sub>2–x</sub>Se NCs is clearly visualized. To demonstrate the time-dependent Au–Cu<sub>2–x</sub>Se accumulation, the PA signal amplitudes in the SLN were spatially averaged. Figure 4I shows the change in PA signal vs time after the injection. The PA signal amplitude at the SLN gradually increased over time, implying that Au–Cu<sub>2–x</sub>Se NCs gradually accumulated in the SLN, approaching saturation about 197 min after the injection. The PA signal was enhanced by  $437 \pm 7\%$  at 251 min postinjection.

To validate our in vivo imaging results, we photoacoustically imaged excised lymph nodes (L1–3; L1, SLN) from the axillary region of the rat where we had injected the Au–Cu<sub>2–x</sub>Se NCs, as shown in Figure 5A and B. As a control, normal lymph nodes (L4–6) were obtained from the other side of the axillae. Only the excised lymph nodes from the injection site are visualized in

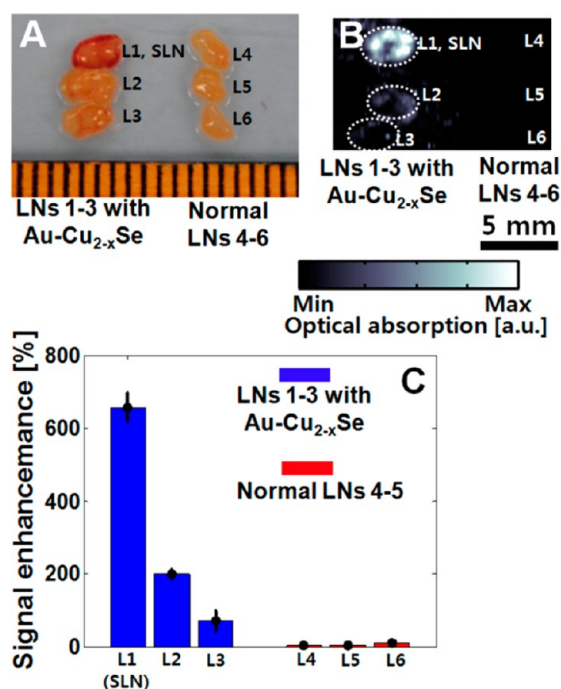


**Figure 5.** (A) Photograph and (B) PA MAP image of the excised lymph nodes (LNs) after injection of Au-Cu<sub>2-x</sub>Se NCs (L1–3) and the normal LNs (L4–6) ex vivo. L1 is the sentinel lymph node (SLN). (C) Quantification of the PA amplitudes measured from the excised LNs.

the PA image, whereas others dissected from noninjection site are not (Figure 5B). Not surprisingly, the strongest PA signal was generated from the SLN. The quantified signal enhancement compared to background was  $651 \pm 41\%$  (Figure 5C). Further, the axillary lymph node chain was observed in vivo and validated by ex vivo imaging. Thus, these results demonstrate

the feasibility of using Au-Cu<sub>2-x</sub>Se NCs for PA mapping of lymph nodes.

To assess the capability of PA mapping of SLNs in clinical practice, the imaging depth was increased by adding chicken tissue on top of the rat. Figure 6A shows the in vivo depth-sensitive PA B-scan image of the SLN after injection of Au-Cu<sub>2-x</sub>Se NPs without addition of chicken tissue. The SLN was clearly visible in the image and was located  $\sim 2$  mm beneath the skin surface. Then, the imaging depth was incremented to 7 (Figure 6B), 12 (Figure 6C), and 17 (Figure 6D) mm, by stacking three individual chicken tissue slices. To improve the signal-to-noise ratio (SNR), the PA amplitudes were averaged 30 times. Because the typical location of SLNs in human breasts is  $\sim 12 \pm 5$  mm beneath the skin surface,<sup>49</sup> the depth of 17 mm achieved here is of important clinical relevance. Figure 6E is a plot of the PA amplitude as a function of the imaging depth of the SLN. The PA signal decreased exponentially with increasing depth. The calculated 1/e penetration depth in chicken tissue is approximately 0.57 cm at an optical wavelength of 1064 nm. The reported penetration depth for 1/e decay in human breast is 0.53 cm at 980 nm, which agrees well with our measurement.<sup>50</sup> Note that we used a laser fluence of  $\sim 10$  mJ/cm<sup>2</sup>, which is only 1/10 of the ANSI safety limit. We expect that the penetration depth could be extended even further using the maximum allowable laser fluence.

To investigate the dynamics of Au-Cu<sub>2-x</sub>Se NCs in the circulatory system, we monitored the change in PA signal within the rat axillary vasculature after two successive intravenous injections of Au-Cu<sub>2-x</sub>Se NCs (4 mg/mL and 200  $\mu$ L total) in vivo. Figure 7 parts A and B were obtained before and after the injection of Au-Cu<sub>2-x</sub>Se NCs, respectively. Figure 7B shows the axillary vasculature with greater clarity due to the injected extrinsic contrast agent, compared with Figure 7A, which only shows intrinsic contrast. Further, we quantified the increase in PA signals after the injection (Figure 7C). First, the signal within the region of interest (ROI) was integrated over each image and then normalized to that of the control

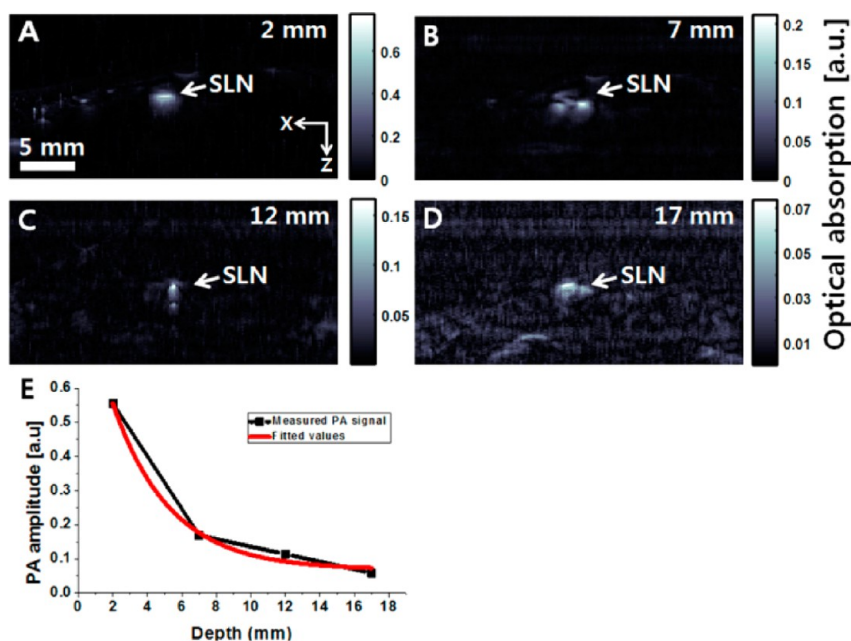


**Figure 6.** In vivo noninvasive PA imaging of rat sentinel lymph node (SLNs) at various depths: (A) 2 mm, (B) 7 mm, (C) 12 mm, and (D) 17 mm. The imaging depth was increased by overlaying chicken tissue atop the rat. (E) Plot of PA amplitudes vs imaging depth of the SLN.



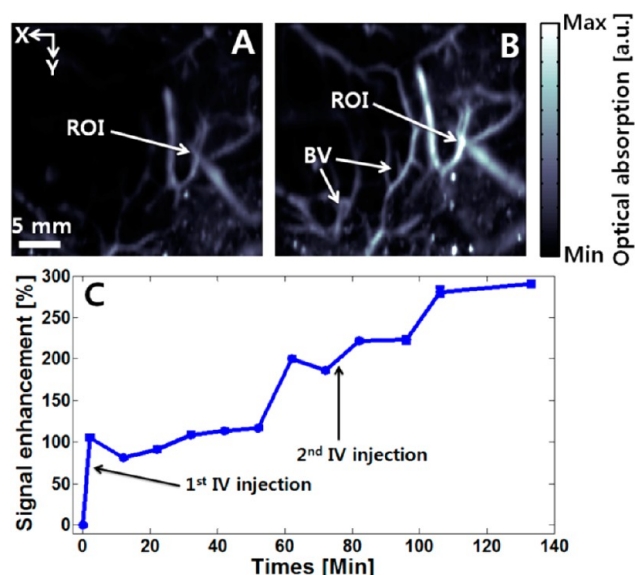


**Figure 7.** In vivo noninvasive PA images of rat axillary vasculatures (A) before and (B) about 2 h after the intravenous (IV) injection of Au–Cu<sub>2–x</sub>Se NCs. (C) The integrated PA signal enhancement estimated from the experimental images during the two-successive-injection experiment, ROI, region of interest.

image. Compared to the control signal, the PA signal was enhanced by ~200%, which appeared about 1 h after the first injection. Moreover, the signal was even further enhanced by ~290% about 1 h after the second injection.

In conclusion, we have synthesized Au–Cu<sub>2–x</sub>Se nanodimers using the seeded-growth method and demonstrated their utility for high contrast multimodal imaging in vitro and in vivo. Their optical properties are characterized by a plasmonic peak in the visible spectral range, and an exceptionally flat NIR absorption profile. The underlying plasmonic interaction between semiconductor and metallic nanostructures demonstrated here opens up a new approach for tuning plasmon resonance absorption spectra across a broad wavelength range in extremely small nanostructures, that is, without creating nanorods, nanoshells, nanocages, or other complex structures. The broad LSPR absorbance enables both dark-field optical imaging and PA imaging with different light sources. The clinical relevance of these new PA contrast agents was demonstrated through deep tissue visualization of a SLN in a rat. Imaging through layers of chicken breast tissue at total imaging depths needed for human SLN imaging was achieved. Further, the kinetics of these NCs in the rat circulatory system were successfully monitored in vivo. A widely available and relatively low cost Nd:YAG laser source (1064 nm) was used for all PA imaging experiments, which is an additional benefit for easy commercialization and clinical translation. Thus, these unique Au–Cu<sub>2–x</sub>Se heterodimer NPs provide a promising optical contrast agent for deep tissue imaging by PAT, as well as a new material system for fundamental studies of plasmonic interactions. In future work, we will use theory and simulations to develop a more quantitative understanding of the interactions of the plasmonic metal and heavily doped semiconductor domains, test the generality of this approach using other metals and semiconductors, and explore the applicability of these materials for photothermal therapy as well as imaging.

## ■ ASSOCIATED CONTENT

### § Supporting Information

Detailed materials and methods, including Figures S1–S9. This material is available free of charge via the Internet at <http://pubs.acs.org>.

## ■ AUTHOR INFORMATION

### Corresponding Authors

\*E-mail: [swihart@buffalo.edu](mailto:swihart@buffalo.edu).

\*E-mail: [chulhong@postech.edu](mailto:chulhong@postech.edu).

\*E-mail: [pnprasad@buffalo.edu](mailto:pnprasad@buffalo.edu).

### Author Contributions

X.L., C.L., and W.-C.L. contributed equally to this work.

### Notes

The authors declare no competing financial interest.

## ■ ACKNOWLEDGMENTS

This work was supported in part by SUNY Buffalo startup funds, IT Consilience Creative Program of MKE and NIPA (NIPA-2013-H0203-13-1001), and NRF grant of Korea government (MSIP) (2011-0030075) to C.K.

## ■ REFERENCES

- (1) Bruchez, M.; Moronne, M.; Gin, P.; Weiss, S.; Alivisatos, A. P. Semiconductor nanocrystals as fluorescent biological labels. *Science* **1998**, *281*, 2013–2016.
- (2) Chan, W. C. W.; Nie, S. M. Quantum dot bioconjugates for ultrasensitive nonisotopic detection. *Science* **1998**, *281*, 2016–2018.
- (3) Yavuz, M. S.; Cheng, Y. Y.; Chen, J. Y.; Cobley, C. M.; Zhang, Q.; Rycenga, M.; Xie, J. W.; Kim, C.; Song, K. H.; Schwartz, A. G.; Wang, L. H. V.; Xia, Y. N. Gold nanocages covered by smart polymers for controlled release with near-infrared light. *Nat. Mater.* **2009**, *8*, 935–939.
- (4) Prasad, P. N. *Introduction to biophotonics*; Wiley-Interscience: Hoboken, NJ, 2003.
- (5) Prasad, P. N. *Introduction to nanomedicine and nanobioengineering*; John Wiley & Sons: Hoboken, NJ, 2012.
- (6) Chen, Y. S.; Frey, W.; Kim, S.; Kruizinga, P.; Homan, K.; Emelianov, S. Silica-Coated Gold Nanorods as Photoacoustic Signal Nanoamplifiers. *Nano Lett.* **2011**, *11*, 348–354.
- (7) Xia, Y. N.; Li, W. Y.; Cobley, C. M.; Chen, J. Y.; Xia, X. H.; Zhang, Q.; Yang, M. X.; Cho, E. C.; Brown, P. K. Gold Nanocages: From Synthesis to Theranostic Applications. *Acc. Chem. Res.* **2011**, *44*, 914–924.
- (8) Choi, H. S.; Liu, W.; Misra, P.; Tanaka, E.; Zimmer, J. P.; Ipe, B. I.; Bawendi, M. G.; Frangioni, J. V. Renal clearance of quantum dots. *Nat. Biotechnol.* **2007**, *25*, 1165–1170.
- (9) Yong, K. T.; Qian, J.; Roy, I.; Lee, H. H.; Bergey, E. J.; Trampusch, K. M.; He, S. L.; Swihart, M. T.; Maitra, A.; Prasad, P. N. Quantum rod bioconjugates as targeted probes for confocal and two-photon fluorescence imaging of cancer cells. *Nano Lett.* **2007**, *7*, 761–765.
- (10) Cai, W. B.; Shin, D. W.; Chen, K.; Gheysens, O.; Cao, Q. Z.; Wang, S. X.; Gambhir, S. S.; Chen, X. Y. Peptide-labeled near-infrared quantum dots for imaging tumor vasculature in living subjects. *Nano Lett.* **2006**, *6*, 669–676.
- (11) Huang, J.; Bu, L. H.; Xie, J.; Chen, K.; Cheng, Z.; Li, X. G.; Chen, X. Y. Effects of Nanoparticle Size on Cellular Uptake and Liver MRI with Polyvinylpyrrolidone-Coated Iron Oxide Nanoparticles. *ACS Nano* **2010**, *4*, 7151–7160.
- (12) Gao, J. H.; Gu, H. W.; Xu, B. Multifunctional Magnetic Nanoparticles: Design, Synthesis, and Biomedical Applications. *Acc. Chem. Res.* **2009**, *42*, 1097–1107.
- (13) Lee, J. H.; Lee, K.; Moon, S. H.; Lee, Y.; Park, T. G.; Cheon, J. All-in-One Target-Cell-Specific Magnetic Nanoparticles for Simulta-

neous Molecular Imaging and siRNA Delivery. *Angew. Chem., Int. Ed.* **2009**, *48*, 4174–4179.

(14) Gao, X. H.; Cui, Y. Y.; Levenson, R. M.; Chung, L. W. K.; Nie, S. M. *In vivo* cancer targeting and imaging with semiconductor quantum dots. *Nat. Biotechnol.* **2004**, *22*, 969–976.

(15) Fu, A. H.; Gu, W. W.; Bousset, B.; Koski, K.; Gerion, D.; Manna, L.; Le Gros, M.; Larabell, C. A.; Alivisatos, A. P. Semiconductor quantum rods as single molecule fluorescent biological labels. *Nano Lett.* **2007**, *7*, 179–182.

(16) Chen, J.; Saeki, F.; Wiley, B. J.; Cang, H.; Cobb, M. J.; Li, Z. Y.; Au, L.; Zhang, H.; Kimmey, M. B.; Li, X. D.; Xia, Y. N. Gold nanocages: Bioconjugation and their potential use as optical imaging contrast agents. *Nano Lett.* **2005**, *5*, 473–477.

(17) Huang, X. H.; El-Sayed, I. H.; Qian, W.; El-Sayed, M. A. Cancer cell imaging and photothermal therapy in the near-infrared region by using gold nanorods. *J. Am. Chem. Soc.* **2006**, *128*, 2115–2120.

(18) Lal, S.; Clare, S. E.; Halas, N. J. Nanoshell-Enabled Photothermal Cancer Therapy: Impending Clinical Impact. *Acc. Chem. Res.* **2008**, *41*, 1842–1851.

(19) Allen, P. M.; Bawendi, M. G. Ternary I-III-VI quantum dots luminescent in the red to near-infrared. *J. Am. Chem. Soc.* **2008**, *130*, 9240.

(20) Xie, R. G.; Rutherford, M.; Peng, X. G. Formation of High-Quality I-III-VI Semiconductor Nanocrystals by Tuning Relative Reactivity of Cationic Precursors. *J. Am. Chem. Soc.* **2009**, *131*, 5691–5697.

(21) Gobin, A. M.; Lee, M. H.; Halas, N. J.; James, W. D.; Drezek, R. A.; West, J. L. Near-infrared resonant nanoshells for combined optical imaging and photothermal cancer therapy. *Nano Lett.* **2007**, *7*, 1929–1934.

(22) Chen, J. Y.; Glaus, C.; Laforest, R.; Zhang, Q.; Yang, M. X.; Gidding, M.; Welch, M. J.; Xia, Y. N. Gold Nanocages as Photothermal Transducers for Cancer Treatment. *Small* **2010**, *6*, 811–817.

(23) Wei, Q. S.; Wei, A. Optical Imaging with Dynamic Contrast Agents. *Chem.—Eur. J.* **2011**, *17*, 1080–1091.

(24) Law, W. C.; Yong, K. T.; Roy, I.; Xu, G.; Ding, H.; Bergey, E. J.; Zeng, H.; Prasad, P. N. Optically and magnetically doped organically modified silica nanoparticles as efficient magnetically guided biomarkers for two-photon imaging of live cancer cells. *J. Phys. Chem. C* **2008**, *112*, 7972–7977.

(25) Erogbogbo, F.; Yong, K. T.; Hu, R.; Law, W. C.; Ding, H.; Chang, C. W.; Prasad, P. N.; Swihart, M. T. Biocompatible Magnetofluorescent Probes: Luminescent Silicon Quantum Dots Coupled with Superparamagnetic Iron(III) Oxide. *ACS Nano* **2010**, *4*, 5131–5138.

(26) Park, J. H.; von Maltzahn, G.; Ruoslahti, E.; Bhatia, S. N.; Sailor, M. J. Micellar hybrid nanoparticles for simultaneous magnetofluorescent imaging and drug delivery. *Angew. Chem., Int. Ed.* **2008**, *47*, 7284–7288.

(27) Xu, C.; Xie, J.; Ho, D.; Wang, C.; Kohler, N.; Walsh, E. G.; Morgan, J. R.; Chin, Y. E.; Sun, S. Au-Fe<sub>3</sub>O<sub>4</sub> dumbbell nanoparticles as dual-functional probes. *Angew. Chem., Int. Ed.* **2008**, *47*, 173–176.

(28) Jin, Y. D.; Jia, C. X.; Huang, S. W.; O'Donnell, M.; Gao, X. H. Multifunctional nanoparticles as coupled contrast agents. *Nat. Commun.* **2010**, *1*, 41.

(29) Mokari, T.; Rothenberg, E.; Popov, I.; Costi, R.; Banin, U. Selective growth of metal tips onto semiconductor quantum rods and tetrapods. *Science* **2004**, *304*, 1787–1790.

(30) Shi, W. L.; Zeng, H.; Sahoo, Y.; Ohulchanskyy, T. Y.; Ding, Y.; Wang, Z. L.; Swihart, M.; Prasad, P. N. A general approach to binary and ternary hybrid nanocrystals. *Nano Lett.* **2006**, *6*, 875–881.

(31) Shaviv, E.; Schubert, O.; Alves-Santos, M.; Goldoni, G.; Di Felice, R.; Vallee, F.; Del Fatti, N.; Banin, U.; Sonnichsen, C. Absorption Properties of Metal-Semiconductor Hybrid Nanoparticles. *ACS Nano* **2011**, *5*, 4712–4719.

(32) Khon, E.; Mereshchenko, A.; Tarnovsky, A. N.; Acharya, K.; Klinkova, A.; Hewa-Kasakarage, N. N.; Nemitz, I.; Zamkov, M. Suppression of the Plasmon Resonance in Au/CdS Colloidal Nanocomposites. *Nano Lett.* **2011**, *11*, 1792–1799.

(33) Luther, J. M.; Jain, P. K.; Ewers, T.; Alivisatos, A. P. Localized surface plasmon resonances arising from free carriers in doped quantum dots. *Nat. Mater.* **2011**, *10*, 361–366.

(34) Zhao, Y. X.; Pan, H. C.; Lou, Y. B.; Qiu, X. F.; Zhu, J. J.; Burda, C. Plasmonic Cu<sub>2-x</sub>S Nanocrystals: Optical and Structural Properties of Copper-Deficient Copper(I) Sulfides. *J. Am. Chem. Soc.* **2009**, *131*, 4253–4261.

(35) Liu, X.; Wang, X. L.; Zhou, B.; Law, W. C.; Cartwright, A. N.; Swihart, M. T. Size-Controlled Synthesis of Cu<sub>2-x</sub>E (E = S, Se) Nanocrystals with Strong Tunable Near-Infrared Localized Surface Plasmon Resonance and High Conductivity in Thin Films. *Adv. Funct. Mater.* **2013**, *23*, 1256–1264.

(36) Dorfs, D.; Hartling, T.; Misztal, K.; Bigall, N. C.; Kim, M. R.; Genovese, A.; Falqui, A.; Povia, M.; Manna, L. Reversible Tunability of the Near-Infrared Valence Band Plasmon Resonance in Cu<sub>2-x</sub>Se Nanocrystals. *J. Am. Chem. Soc.* **2011**, *133*, 11175–11180.

(37) Liu, X.; Law, W. C.; Jeon, M.; Wang, X. L.; Liu, M.; Kim, C.; Prasad, P. N.; Swihart, M. T. Cu<sub>2-x</sub>Se Nanocrystals with Localized Surface Plasmon Resonance as Sensitive Contrast Agents for *In Vivo* Photoacoustic Imaging: Demonstration of Sentinel Lymph Node Mapping. *Adv. Healthcare Mater.* **2013**, *2*, 952–7.

(38) Kim, C.; Favazza, C.; Wang, L. H. V. *In Vivo* Photoacoustic Tomography of Chemicals: High-Resolution Functional and Molecular Optical Imaging at New Depths. *Chem. Rev.* **2010**, *110*, 2756–2782.

(39) Wang, X. D.; Pang, Y. J.; Ku, G.; Xie, X. Y.; Stoica, G.; Wang, L. H. V. Noninvasive laser-induced photoacoustic tomography for structural and functional *in vivo* imaging of the brain. *Nat. Biotechnol.* **2003**, *21*, 803–806.

(40) Agarwal, A.; Shao, X.; Rajian, J. R.; Zhang, H. A.; Chamberland, D. L.; Kotov, N. A.; Wang, X. D. Dual-mode imaging with radiolabeled gold nanorods. *J. Biomed. Opt.* **2011**, *16*, 051307.

(41) Lu, W.; Huang, Q.; Geng, K. B.; Wen, X. X.; Zhou, M.; Guzatov, D.; Brecht, P.; Su, R.; Oraevsky, A.; Wang, L. V.; Li, C. Photoacoustic imaging of living mouse brain vasculature using hollow gold nanospheres. *Biomaterials* **2010**, *31*, 2617–2626.

(42) Kim, C.; Song, H. M.; Cai, X.; Yao, J. J.; Wei, A.; Wang, L. H. V. *In vivo* photoacoustic mapping of lymphatic systems with plasmon-resonant nanostars. *J. Mater. Chem.* **2011**, *21*, 2841–2844.

(43) Wang, X. D.; Ku, G.; Wegiel, M. A.; Bornhop, D. J.; Stoica, G.; Wang, L. H. V. Noninvasive photoacoustic angiography of animal brains *in vivo* with near-infrared light and an optical contrast agent. *Opt. Lett.* **2004**, *29*, 730–732.

(44) Ku, G.; Wang, X. D.; Xie, X. Y.; Stoica, G.; Wang, L. H. V. Imaging of tumor angiogenesis in rat brains *in vivo* by photoacoustic tomography. *Appl. Opt.* **2005**, *44*, 770–775.

(45) de la Zerda, A.; Liu, Z. A.; Bodapati, S.; Teed, R.; Vaithilingam, S.; Khuri-Yakub, B. T.; Chen, X. Y.; Dai, H. J.; Gambhir, S. S. Ultrahigh Sensitivity Carbon Nanotube Agents for Photoacoustic Molecular Imaging in Living Mice. *Nano Lett.* **2010**, *10*, 2168–2172.

(46) Song, K. H.; Kim, C. H.; Cobley, C. M.; Xia, Y. N.; Wang, L. V. Near-Infrared Gold Nanocages as a New Class of Tracers for Photoacoustic Sentinel Lymph Node Mapping on a Rat Model. *Nano Lett.* **2009**, *9*, 183–188.

(47) Talley, C. E.; Jackson, J. B.; Oubre, C.; Grady, N. K.; Hollars, C. W.; Lane, S. M.; Huser, T. R.; Nordlander, P.; Halas, N. J. Surface-enhanced Raman scattering from individual Au nanoparticles and nanoparticle dimer substrates. *Nano Lett.* **2005**, *5*, 1569–1574.

(48) Parasuraman, S.; Raveendran, R.; Kesavan, R. Blood sample collection in small laboratory animals. *J. Pharmacol. Pharmacother.* **2010**, *1*, 87–93.

(49) Song, K. H.; Stein, E. W.; Margenthaler, J. A.; Wang, L. V. Noninvasive photoacoustic identification of sentinel lymph nodes containing methylene blue *in vivo* in a rat model. *J. Biomed. Opt.* **2008**, *13*, 054033.

(50) Spinelli, L.; Torricelli, A.; Pifferi, A.; Taroni, P.; Danesini, G. M.; Cubeddu, R. Bulk optical properties and tissue components in the female breast from multiwavelength time-resolved optical mammography. *J. Biomed. Opt.* **2004**, *9*, 1137–1142.